Controlling Toughness of Polymer-grafted Nanoparticle Composites for Impact Mitigation

Shawn H. Chen,[a] Amanda J. Souna,[b] Stephan J. Stranick,[a] Mayank Jhalaria,[c] Sanat K. Kumar,[c] Christopher L. Soles, and [b] Edwin P. Chan[b*]

[a] *Materials Measurement Science Division, NIST, Gaithersburg, MD 20899*
[b] *Materials Science and Engineering Division, NIST, Gaithersburg, MD 20899*
[c] *Department of Chemical Engineering, Columbia University, New York, NY 10027*

1 Methods

Certain commercial equipment, instruments, or materials are identified in this paper in order to specify the experimental procedure adequately. Such identification is not intended to imply recommendation or endorsement by NIST, nor is it intended to imply that the materials or equipment identified are necessarily the best available for the purpose.

1.1 PGN Films for LIPIT

PMA-grafted SiO_2 nanoparticles (PGN) were prepared using the procedure described in Refs.[1–3]. Table 1 summarizes the properties of the PGNs. Briefly, solid PGN were dissolved in a mixed solvent of toluene and tetrahydrofuran by stirring overnight with a Teflon stir bar to obtain solutions with concentrations between 25 mg/mL to 120 mg/mL depending on the PMA molecular mass. Thin films were fabricated by spin-coating the prepared solutions at 4000 rpm for 10 s onto UV-Ozone cleaned silicon wafers that have been coated with a sacrificial layer of 1 % by mass aqueous solution of poly(styrene sulfonate). Film thicknesses were measured with a 3D optical profilometer (KLA-Tencor, Milpitas, CA). Previous work have investigated contribution of decreasing film thickness and confinement effects on molecular mobility and Tg.[4] While we've investigated and discussed film thickness effects at high impact rates previously,[5] here we selected these film thicknesses, which we considered to be "bulk-like", to investigate the molecular contributions to energy dissipation as a function of molecular mass. The glass transition temperatures (T_g) of the PGNs and the neat PMAs as a function of molecular mass of the PMA are shown in S3. For the PGNs, $T_g \approx 17$ °C across the molecular mass range investigated.

Sample name	**Molecular mass of grafted chain** M_w (kg/mol.)	**Graft density** Σ (chains/nm^2)	**SiO_2 core radius** R_o (nm)	**PGN radius*** R_{tot}(nm)	**Vol. frac. of core*** ϕ_o	**Film thickness** l (nm)
31K	31	0.47	8	16.32	0.118	370
55K	55	↓	↓	19.42	0.069	415
82K	82	↓	↓	22.02	0.048	370
96K	96	↓	↓	23.15	0.041	375
111K	111	↓	↓	24.25	0.036	383
122K	122	↓	↓	25.00	0.033	385
184K	184	↓	↓	28.56	0.022	364

Table 1: Summary of the molecular characteristics of PMA-grafted SiO_2 nanoparticles (PGN). *R_{tot} and ϕ_o were estimated based on the two-layer model by Midya and coworkers.[6] Specifically, R_{tot} was determined using Eq.(28) below and $\phi_o = R_o^3/R_{tot}^3$.

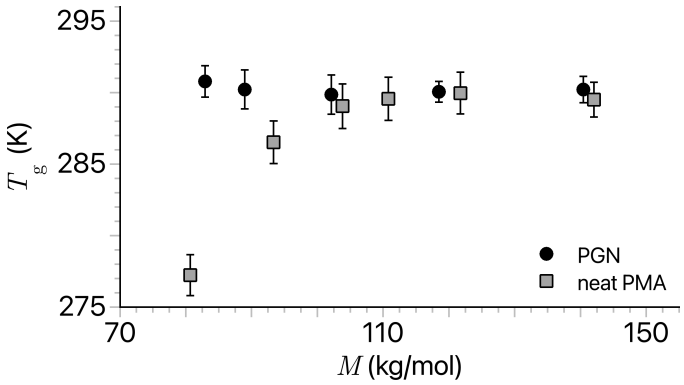

Figure S1: Glass transition temperatures (T_g) as a function of molecular mass of the PGN and neat PMA materials.

Dried films were cut into 2 by 2 mm squares with a razor blade, floated in ice cold water onto TEM grids, and dried under vacuum for 3 hours. Samples were stored in a refrigerator when not in use and all tested within 12 hours of preparation.

1.2 Ablation Target Preparation

Ablation targets were prepared using microscope glass coverslips sputter-coated with a 40 nm layer of gold and blade-coated with a 60 μm layer of polydimethylsiloxane (PDMS, Sylgard 184). The PDMS was used in a 10:1 mass ratio of prepolymer to catalyst, degassed before blade-coating, and cured at 120 °C for 15 minutes. 28 μm diameter lime glass spheres (Cospheric Inc) were directly distributed onto the PDMS substrate and dispersed with a burst of compressed air to achieve a monolayer of spheres.

1.3 LIPIT Measurement

Microprojectiles were launched using a pulsed diode-pumped solid state 1030-nm laser (Coherent, Flare NX) in single pulse mode to direct a 1.5 ns pulse towards a single glass microsphere on the ablation target. Using a video camera (PixeLINK) and a 20X objective (SLMPLN20x, NA = 0.25, Olympus) for viewing, each microsphere on the ablation target and the center of each section of the PGN film on the TEM grid, were both moved to the position of the laser's focal point using motorized linear stages (Physik Instrumente). Microprojectiles were measured to be 28 $\pm$ 1 μm using the same video camera. The pulse was directed up towards the target, ablating the gold layer. The gold plume propelled the elastomeric PDMS layer upward to launch the projectile towards the PGN film positioned 1 mm above the target. The velocity was adjusted by controlling the pulse energy of the ablation laser.

The images of the microprojectile trajectory were recorded using a diode-pumped, pulsed, 1035-nm laser (Coherent, Monaco) with a pulse length of 300 fs as a stroboscopic illumination source. The laser pulses were frequency-doubled using a BBO crystal, and gated to create a burst of 10 to 20 green (517.5-nm) pulses at a repetition rate of 2 MHz, or 1 pulse every 500 ns. The burst of pulses was used to capture a series of positions in the projectile's trajectory before and after penetration of the film within a single exposure using a scientific complimentary metal-oxide-semiconductor (sCMOS, PCO Edge 4.2, PCO) camera. The ablation laser pulse, the imaging laser pulses, and the camera exposure were timed using digital triggers modulated using a digital waveform generator (NI9402, National Instruments). Using the calibrated distances between successive projectile images and the time between laser pulses, the projectile velocities were calculated at each position.

2 Energy Dissipation Parameters from LIPIT

The incident (v_i) and residual (v_r) velocities were determined from the microprojectile's spatial trajectory and the time increments between positions defined by the repetition rate of laser used for stroboscopic imaging.[7] The kinetic

energy loss (ΔE_k) can then be calculated using,

$$\begin{aligned}\Delta E_\mathrm{k} &= \frac{1}{2} m_\mathrm{p}(v_\mathrm{i}^2 - v_\mathrm{r}^2) \\ &= E_\mathrm{drag} + E_\mathrm{ad} + E_\mathrm{xfer} + E_\mathrm{d} \\ &= E_\mathrm{drag} + E_\mathrm{ad} + E_\mathrm{p}\end{aligned} \tag{1}$$

where m_p is the mass of the microprojectile. ΔE_k includes various mechanisms of energy dissipation including air drag (E_drag), adiabatic work (E_ad), kinetic energy transfer (E_xfer) and energy dissipation by the PGN film (E_d). For our testing conditions, we assume E_drag and E_ad to be negligible as they are ≈ 2 % and ≈ 5 %, respectively, of the incident kinetic energy.[5] Therefore, Eq.(1) can be simplified to,

$$\Delta E_\mathrm{k} \approx E_\mathrm{p} = \frac{m_\mathrm{f}}{2} v_\mathrm{i}^2 + E_\mathrm{d} \tag{2}$$

The first term (E_xfer) is the kinetic energy transferred to a plug of film with mass $m_\mathrm{f} = \rho_\mathrm{f} A l$. Here, ρ_f is the mass density of the film, $A = \pi a_\mathrm{p}^2$ is the area of the plug, a_p is the radius of the microprojectile, and the l is the film thickness. E_d represents the other mechanisms of energy dissipation specific to the material.

To compare the performance between different materials, the specific puncture energy (E_p^*) is used instead as it is normalized by the mass of the plug of material that contributed to energy dissipation.

$$E_\mathrm{p}^* = \frac{E_\mathrm{p}}{m_\mathrm{f}} = \frac{v_\mathrm{i}^2}{2} + E_\mathrm{d}^* \tag{3}$$

2.1 LIPIT Deformation Time

We can estimate the deformation time of LIPIT experiments based on the cone velocity (v_c) of the microballistic impact event. It is related to the in-plane speed of sound for the polymer ($c_\parallel$),

$$v_\mathrm{c} \cong 1.23 c_\parallel \left(\frac{v_\mathrm{i}}{2^{1/2} c_\parallel} \right)^{2/3} \tag{4}$$

Specifically, the deformation time (t_p) is defined as,

$$t_\mathrm{p} \cong \frac{L_\mathrm{max}}{v_\mathrm{c}} \tag{5}$$

where L_max is the maximum radius of the expanding cone-shaped deformation region. For v_i= 100 m s^{-1} and $L_\mathrm{max} \approx$ 80 μm estimated from the post-punctured images, we get: $v_\mathrm{c} \cong 220$ m s^{-1} and $t_\mathrm{p} \cong 364$ ns with $c_{||} \approx 114$ m s^{-1} for pure PMA.[8]

3 Application of Wool's Percolation Model of Polymer Fracture

Wool presents an alternative approach in understanding the molecular contributions to polymer fracture based on the rigidity percolation (RP) theory.[9] Here, the making and breaking of bonds in entangled polymers is parameterized based on connectivity of a percolated "network". In RP, the material is treated as a collection of bonds and nodes randomly arranged in space. The transmission of mechanical forces through the material is defined by the fraction of bonds (p) that is load bearing. The elastic modulus (E) is defined as,

$$E \sim (p - p_\mathrm{c})^n \tag{6}$$

where p_c is the percolation threshold and n is the vector percolation exponent. Note that Eq.(6) defines the elasticity of the material with contributions from both bond stretching and angle bending of the bonds.

Importantly, this model is directly relevant to describing the fracture of a polymer. **First**, the random connectivity of the "network" results in a nonuniform stress distribution. Certain bonds are highly stressed whereas others are

not load bearing at all. The existence of highly stressed bonds is the basis for understanding why polymers fail under stresses that are much lower than the theoretical fracture stress of a covalent bond. **Second**, only a fraction of the bonds ($= p - p_c$) needs to be broken before complete failure occurs. For polymer fracture, the crack advances through the deformation zone (i.e., a volume of material ahead of the crack tip) by breaking a fraction of bonds that are randomly distributed within this zone since it contains a significant number of defects that are randomly distributed. **Third**, the network connectivity must exceed the percolation threshold ($p > p_c$) for strength to develop. When $p < p_c$, the connectivity of the bonds are broken and there is no significant strength in the material beyond weak secondary interactions. For polymers, this implies that the polymer parameters (i.e. molecular mass, areal density of chains, entanglements, etc) must satisfy the percolation threshold requirement as well.

When a uniaxial tensile stress (σ) is applied to the material, the stored elastic strain energy density ($W \equiv$ energy/volume) is defined as,

$$W = \frac{\sigma^2}{2E} \tag{7}$$

The elastic modulus relative to that of a perfect network ($p = 1$) is,

$$E = E_0 \left(\frac{p - p_c}{1 - p_c} \right)^n \tag{8}$$

The strain energy density function as a function of multiaxial stretch (λ_i) for elastomers can be defined by the Mooney equation,

$$W(\lambda_1, \lambda_2, \lambda_3) = C_1(\lambda_1^2 + \lambda_2^2 + \lambda_3^2 - 3) + C_2(\lambda_1^{-2} + \lambda_2^{-2} + \lambda_3^{-2} - 3) \tag{9}$$

where C_1 and C_2 are elastic constants of the material. According to Flory's theory of rubber elasticity, $C_2 = 0$ and $\lambda_1\lambda_2\lambda_3 = 1$ (i.e. material is incompressible), the strain energy density for uniaxial tension simplifies to,

$$W(\lambda_1) = C_1 \left(\lambda_1^2 + \frac{2}{\lambda_1} - 3 \right) \tag{10}$$

where C_1 is related to the crosslink density ($\nu_x \equiv$ crosslinks/volume) of the network. The energy required to fracture ($W_f \equiv$ work of fracture) a network consisting of ν bonds with bond dissociation energy U is defined as,

$$W_f = \nu_x U (p - p_c) \tag{11}$$

Fracture occurs when the critical strain energy ($W^* = \sigma^{*2}/2E$) exceeds the work of fracture,

$$W^* \geq W_f \tag{12}$$

The critical fracture stress is determined by substituting Eq.(9) and Eq.(11) into Eq.(12), which yields,

$$\sigma^* = \sqrt{2E\nu_x U(p - p_c)} \tag{13}$$

This equation predicts the following:

1. The critical stress, $\sigma^* \sim \nu_{\mathrm{x}}^{1/2}$.
2. The true crosslink density is the product $\nu_{\mathrm{x}}(p-p_{\mathrm{c}})$ such that for a perfect network without defects, $p=1$. For a network with missing bonds or one that is damaged, $p<1$.
3. As $p \to p_{\mathrm{c}}$, the network becomes very fragile since $\sigma^* \to 0$.

3.1 Fracture of Entangled Polymers: Chain Scission

For an entangled polymer, ν_{x} is replaced with the entanglement density ($\nu_{\mathrm{e}} \approx \rho_{\mathrm{p}} N_{\mathrm{A}}/M_{\mathrm{e}}$ where $\rho_{\mathrm{p}} \equiv$ polymer density and $M_{\mathrm{e}} \equiv$ entanglement molecular mass) such that Eq.(11) becomes

$$W_{\mathrm{f}} = \nu_{\mathrm{e}} U (p - p_{\mathrm{c}}) \tag{14}$$

In the context of percolation theory of an entangled polymer, p can also be defined as the normalized entanglement density. It is related to the number of chains per unit volume (n_{v}) and entanglement density of infinite molecular mass ($\nu_{\mathrm{e},\infty}$),

$$p = \frac{n_{\mathrm{e}}(\lambda) n_{\mathrm{v}}}{\nu_{\mathrm{e},\infty}} \tag{15}$$

The parameter $n_{\mathrm{e}}(\lambda)$ is the number of entanglements per chain as a function of the stretch ratio (λ). Since chain ends leads to the loss of a single entanglement, it is defined as,

$$n_{\mathrm{e}}(\lambda) = \frac{M}{M_{\mathrm{e}}(\lambda)} - 1 \tag{16}$$

Assuming that $n_{\mathrm{v}} \approx \rho_{\mathrm{p}} N_{\mathrm{A}}/M$ and $\nu_{\mathrm{e},\infty} \approx \rho_{\mathrm{p}} N_{\mathrm{A}}/M_{\mathrm{e}}$ yields,

$$\begin{aligned} p &= \frac{\left(\frac{M}{M_{\mathrm{e}}(\lambda)} - 1\right)\rho_{\mathrm{p}} N_{\mathrm{A}}/M}{\rho_{\mathrm{p}} N_{\mathrm{A}}/M_{\mathrm{e}}(\lambda)} \\ &= 1 - \frac{M_e(\lambda)}{M} \end{aligned} \tag{17}$$

where $M_{\mathrm{e}}(\lambda)$ accounts for the fact that the entanglement molecular mass or distance between entanglements increases with stretch. Specifically,

$$M_{\mathrm{e}}(\lambda) = \lambda^2 M_{\mathrm{e}} \tag{18}$$

Substituting Eq.(18) into Eq.(17), we obtain,

$$p = 1 - \lambda^2 \frac{M_e}{M} \tag{19}$$

Eq.(19) will be important if disentanglement is the primary fracture mechanism. For chain scission where the polymer chains have no time to stretch, i.e. $\lambda = 1$, $\implies p = 1 - M_{\mathrm{e}}/M$. Additionally, since $p_{\mathrm{c}} \approx 1/2$,

$$p_{\mathrm{c}} = \frac{1}{2} = 1 - \frac{M_{\mathrm{e}}}{M_{\mathrm{c}}} \tag{20}$$

Thus implying that $M_{\mathrm{c}} \approx 2M_{\mathrm{e}}$.

Substituting Eq.(20) into Eq.(14), the critical strain energy for fracture is,

$$W^* = \frac{2\rho_p N_{\mathrm{A}} U}{M_{\mathrm{c}}} \left(1 - \frac{M_{\mathrm{c}}}{M}\right) \tag{21}$$

Assuming that $W^* \cong G_{\mathrm{c}}$, then

$$G_{\mathrm{c}} = G^*_{\mathrm{sc}} \left(1 - \frac{M_{\mathrm{c}}}{M}\right) \tag{22}$$

which is the prediction for the fracture energy of a glassy polymer undergoing chain scission with $G^*_{\mathrm{sc}} \cong 2\rho_p N_{\mathrm{A}} U/M_{\mathrm{c}}$ defined as the plateau fracture energy value for a polymer of infinitely high molecular mass.

3.2 Fracture of Entangled Polymers: Disentanglement

The disentanglement process is characterized by the stretching of an entangled chain ($M > M_c$) up to a draw ratio (λ). This stretching also causes the average end-to-end distance of entanglement points (R_e) to stretch as well. Assuming affine deformation, the chains will be stretched by λ as well, *i.e.* $R_e(\lambda) = \lambda R_e$.

For $M > M_c$, the critical draw ratio (λ_c) for chain scission can be estimated by equating Eq.(19) with Eq.(20),

$$\lambda_c = \left(2(1-p)\frac{M}{M_c}\right)^{1/2} \sim \left(\frac{M}{M_c}\right)^{1/2} \tag{23}$$

The critical strain energy for fracture due to disentanglement can be defined by substituting Eq.(23) into Eq.(10),

$$\begin{aligned} G_c &\approx E\varepsilon^2 \\ &\sim (\lambda_c - 1)^2 \\ &= 0.3G_d^*\left(\sqrt{\frac{M}{M_c}} - 1\right)^2 \end{aligned} \tag{24}$$

The prefactor $0.3G_d^*$, which was determined based on the limit that at $M = 8M_c, G_d^* = G_c(8M_c) \approx 0.42 \times 8M_c$. Note that Eq.(24) is valid for $M_c \leq M \leq 8M_c$. When $M < M_c$, the contributions of entanglements to the fracture process are not present and Eq.(24) is not applicable. Instead, the Nail solution[10] provides an estimate of the contribution of interpenetrated chain segments to the fracture process.

3.2.1 Entanglement Molecular Mass

The entanglement molecular mass (M_e) can be determined from the shear rheology experiments. For an entangled homopolymer, M_e is related to the shear modulus of the polymer in the rubbery plateau region (μ_e),

$$M_e = \frac{\rho_p RT}{\mu_e} \tag{25}$$

Using the rheology data from Bilchak et al.[2] with $\mu_e \approx 3 \times 10^5$ Pa and $\rho_p = 1.215$ g/cm^3, we estimate $M_e \approx 10$ kg/mol for our PGNs. Since $M_c \approx 2M_e$, $M_c \approx 20$ kg/mol.

3.2.2 Network Failure Time

The disentanglement process is not just a function of the molecular length scale of polymer (M_e), but there is also a time-scale component. Specifically, there must also be commensurability between the deformation rate and the network failure time. Following extension to λ, the chain responds to this deformation and retracts at a rate that is governed by Rouse dynamics, with a network failure time defined as,

$$\tau_f \approx \tau_{RO} \ln(M/M_c) \tag{26}$$

where τ_{RO} is the Rouse time of the polymer chain,[11]

$$\begin{aligned} \tau_{RO} &= \frac{\zeta b^2}{6\pi^2 k_b T}\left(\frac{M}{M_e}\right)^2 \\ &= \frac{2\zeta b^2}{3\pi^2 k_b T}\left(\frac{M}{M_c}\right)^2 \end{aligned} \tag{27}$$

where b is the Kuhn length, and ζ is the monomeric friction coefficient of the polymer, respectively. We estimate ζ of PMA using the relationship, $\zeta \approx k'\tau$.[1] From quasi-elastic neutron scattering experiments of neat PMA,[1] $\tau \approx 120$ ps and $k' \approx 1.9$ N/m, thus $\zeta \cong 2.3 \times 10^{-10}$ N s/m.

Disentanglement is nearly-instantaneous when $M \approx M_c$ and approaches τ_{RO} when $M \approx 8M_c$, which is the upper bound for chain extension ($\lambda = 4$) without chain scission. An important point is that at deformation rates faster than the network failure time, disentanglement cannot occur and the mechanism transitions to chain scission.[9]

3.3 Interpenetration Zone of PGNs

The interpenetrated region is critical to the overall mechanical properties of the PGN as it enables chain entanglements to form. The molecular mass of the grafted chain segment in the interpenetrated region can be determined using the two-layer model proposed by Midya and coworkers.[6] The model assumes that each layer is spherical with: 1) the inner core defined as the radius of the inorganic nanoparticle, 2) middle shell consisting of segments of the grafted polymer chains that are densely packed that cannot interpenetrate, and 3) an outer shell where the chain segments do interpenetrate.

For a nanoparticle with radius R_o decorated with Z polymer grafts, the overall size of the grafted nanoparticle (R_{tot}) is defined as,

$$\frac{4}{3}\pi\Big(R_{tot}^3 - R_o^3\Big) = \frac{ZN}{\rho_m} \tag{28}$$

where N is the number of Kuhn monomers per chain, $\rho_m = \rho_p/(M_m N_A)$ is the average monomer density (= monomer mass/volume), and $Z = 4\pi R_o^2 \rho_g$ with ρ_g being the graft density (= chains/area). The total brush thickness h is,

$$h = R_{tot} - R_o \tag{29}$$

Assuming that the chains in the interpenetrated region are Gaussian, the thickness of the interpenetrated layer is related to the chain dimensions as,

$$h_{inter} = n_{inter}^{1/2} b \tag{30}$$

where b is the Kuhn length. Again using a space filling argument, the size of the interpenetrated layer is,

$$\frac{4}{3}\pi {R_{tot}}^3 - \frac{4}{3}\pi\Big(R_{tot} - \frac{h_{inter}}{2}\Big)^3 = \frac{Z n_{inter}}{\rho_m} \tag{31}$$

3.3.1 Overcrowding Parameter

The overcrowding parameter qualifies the extent of extension of the grafted polymer chains by comparing the volume occupied by Z chains versus the volume occupied by z_{tot} number of unperturbed chains. Specifically, it is defined as,

$$x = \frac{Z}{z_{tot}} \tag{32}$$

where $z_{tot} = \pi \rho_m b^2 R_{tot}$ is defined as the number of unperturbed chains that can occupy the same volume of $\approx \pi R_{tot}^3$.

Substituting Eq.(30) into Eq.(31) and simplifying, n_{inter} is defined as,

$$n_{inter}^{1/2} = \frac{3R_{tot}}{b}(1+x)\left(1 - \sqrt{1 - \frac{4}{3}(1+x)^{-2}}\right) \tag{33}$$

Substituting Eq.(33) into Eq.(30) yields,

$$h_{inter} = R_{tot}\left(2x^{-1} - 2x^{-2} + \frac{8}{3}x^{-3} - 4x^{-4} + ...\right) \tag{34}$$

For our materials, the overcrowding parameter is estimated by considering $R_o = 8$ nm, $\rho_g = 0.47$, and $b = 1.47$ nm. R_{tot} is calculated using Eq.(31) based on the properties of PMA with $N = M/M_m$ and $\rho_m = 8.47$ monomers/nm^3. The monomer mass, $M_m = 86$ g/mol. and the polymer density, $\rho_p = 1.22$ g/cm^3.

The molecular mass of the "dry" brush region can be estimated by comparing M_{inter} with M (**Figure S2**a). A linear fit of the results yields, $M_{inter} = 0.88M - 5.47$. Extrapolating to $M_{inter} = 0$ gives $M_{dry} \approx 6.2$ kg/mol. The number of entanglements increases linearly with M as the chains gain greater degrees of freedom to interdigitate with neighboring chains (**Figure S2**b). When M is low the chain length is insufficiently long to form entanglements, and the conformation represents those in the "dry" brush regime. Chains become less rod-like and more coil-like as x approaches unity, where $x = 1$ represents ideal unperturbed chains in a melt. As indicated in **Figure S2**c, the interpenetrated chains are highly extended, and only at relatively high molecular mass do the chains approach the chain conformation of a polymer melt.

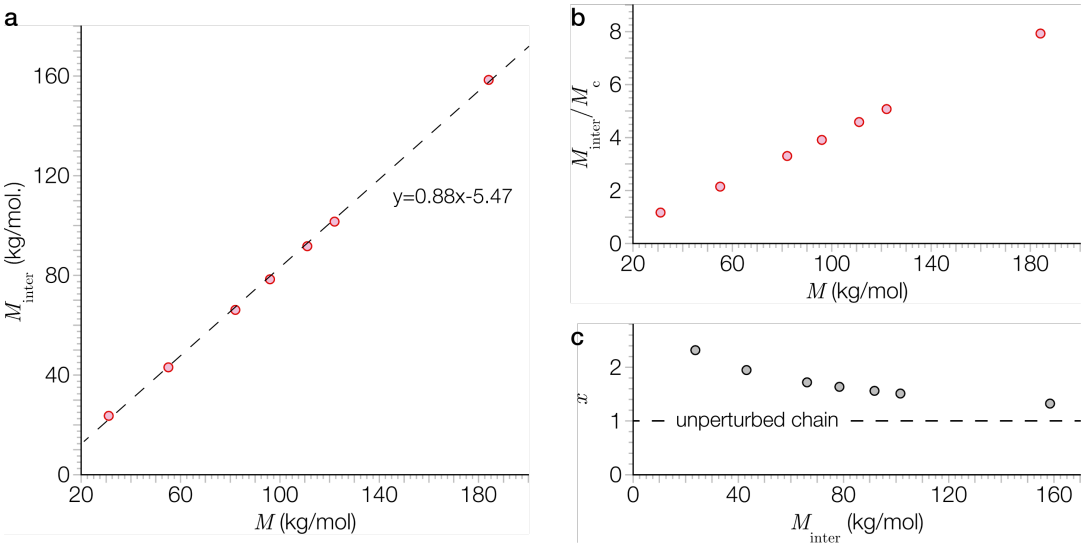

Figure S2: a) Molecular mass of the chain segment in the interpenetrated region (M_{inter}) as a function of molecular mass of the entire chain (M). Extrapolating to $M_{\mathrm{inter}} = 0$ gives $M_{\mathrm{dry}} \approx 6.2$ kg/mol. b) Plot of number of entanglements per chain, estimated using the ratio $M_{\mathrm{inter}}/M_{\mathrm{c}}$, as a function of M. c) Plot of the overcrowding parameter (x) versus M_{inter} indicates that the grafted chains are highly extended across the entire molecular mass series investigated.

3.4 X-ray Photon Correlation Spectroscopy (XPCS)

X-Ray Photon Correlation Spectroscopy (XPCS) experiments were conducted at sector 8-ID-I at the Advanced Photon Source (APS, Argonne national laboratory. 7.35 keV coherent x-rays were used in the experiments, which resulted in an accessible q-range of 0.025 nm^{-1} to 0.063 nm^{-1}. All samples were exposed to identical thermal history prior to the measurements – they were equilibrated at 463 K and then stepped down to the measurement temperature of 393 K. The samples were allowed to equilibrate once again at 393 K prior to the final measurements. Equilibration was tracked by measuring the intensity auto-correlation function with time and waiting for the successive auto-correlation functions to overlap with each other. Once equilibrated, data was collected at five different spots on the sample more than 50 μm apart from each other. This prevents areal overlap between the different points as the nominal beam size was 15 μm $\times$ 5 μm. Independent intensity auto-correlations measured at each of these points overlapped with each other and were averaged prior to curve fitting. Curves at 54 discrete q-vectors were fit with a compressed exponential function $g^{(2)}(q,t) = A(q)(exp(-t/\tau)^{\beta})^2 + 1$, where $\beta > 1$ for all cases considered here. The characteristic decay times is the primary output from these calculations. To account for the compressed nature of the exponential, characteristic decay times were normalized to obtain the mean relaxation time $\langle\tau\rangle = \Gamma(1/\beta)\cdot(\tau/\beta)$, which are plotted as a function of graft chain molecular weight in the main text. As XPCS is a coherent scattering experiment and is related to the decay of the pair correlation function, mean relaxation times were calculated at the first peak of the structure factor for all GNPs.

3.5 Quasi-elastic Neutron Scattering (QENS)

Quasielastic neutron scattering (QENS) experiments were performed on the High Flux Backscattering Spectrometer (HFBS) at the NIST Center for Neutron Research and SPHERES at the Heinz Maier-Leibnitz Zentrum. As both instruments have very similar resolutions, data can be compared across the two. Only the data from the GNP with a MW of 80 kDa was collected on SPHERES.

Films of GNPs were prepared by solvent casting concentrated solutions on to aluminum foil and subsequently evaporating the solvent for 2 days under ambient conditions, and 3 days under vacuum at 353 K. The final film had a thickness of 100 m, which was enough to ensure that neutron transmission was >90%. Elastic scans were performed on the GNP films by first cooling it down to the temperature where all dynamics are frozen (representing a purely elastic scattering medium) and equilibrating at the temperature. Based on instrumental limitations, this temperature was 15 K on HFBS and 4 K on SPHERES. The temperature was ramped at a rate of 1 K/min after equilibration, up to a final temperature of 360 K to 400 K (sample dependent). While ramping, the total number of neutrons scattered elastically were measured at 16 (HFBS) or 10 (SPHERES) discrete wavevectors (or q values) every 1 minute to yield the variation of elastic intensity with temperature and q values for the GNP films.

After discarding the first two q values due to instrumental limitations, the variation of total elastic intensity with q can be fit to extract a Debye-Waller factor ($\langle u^2\rangle$) at each temperature.

$$I = I_0 \exp\Big(\frac{-q^2\langle u^2\rangle}{3}\Big) \tag{35}$$

By treating the system as a harmonic spring, a spring constant can be calculated from the variation of $\langle u^2\rangle$ with temperature and thus $\mathrm{d}\langle u^2\rangle/\mathrm{d}T$ can be used as a proxy to this quantity.

$$k' = \frac{(3\mathrm{k_B}T)}{\frac{\mathrm{d}\langle u^2\rangle}{\mathrm{d}T}} \tag{36}$$

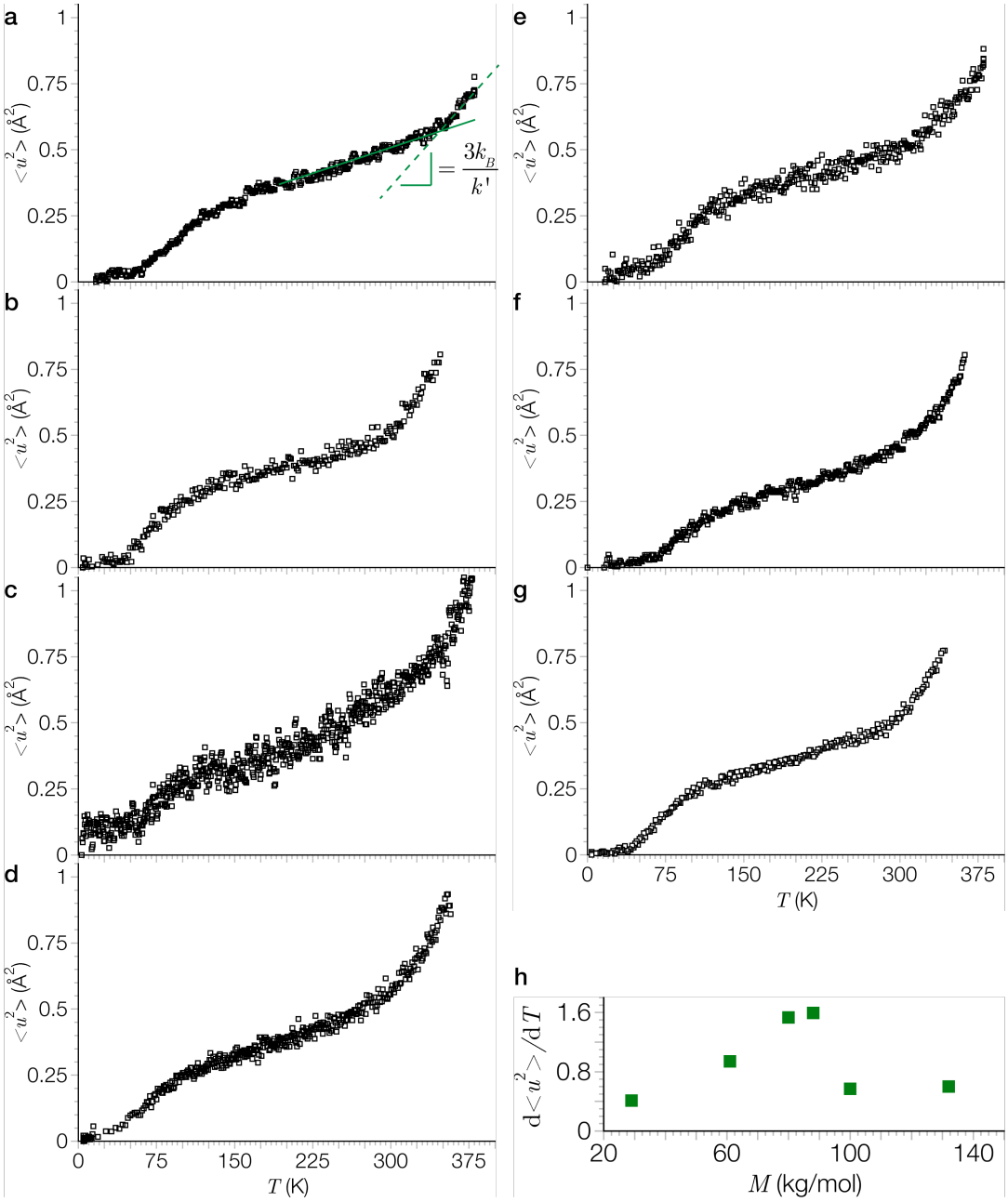

Figure S3: Incoherent elastic neutron scattering results for the PGNs. Mean-squared displacement ($\langle u^2 \rangle$) vs. temperature (T) for a) 29 kg/mol, b) 67 kg/mol, c) 80 kg/mol, d) 88 kg/mol, e) 100 kg/mo., and f) 136 kg/mol. g) Also included is the results for the neat PMA with $M = 63$ kg/mol. h) Plot of $\mathrm{d}\langle u^2 \rangle / \mathrm{d}T$ versus M of the grafted chains.

References

[1] M. Jhalaria, E. Buenning, Y. Huang, M. Tyagi, R. Zorn, M. Zamponi, V. García-Sakai, J. Jestin, B. Benicewicz and S. Kumar, *Phys. Rev. Lett.*, 2019, **123**, 158003.

[2] C. R. Bilchak, E. Buenning, M. Asai, K. Zhang, C. J. Durning, S. K. Kumar, Y. Huang, B. C. Benicewicz, D. W. Gidley, S. Cheng, A. P. Sokolov, M. Minelli and F. Doghieri, *Macromolecules*, 2017, **50**, 7111–7120.

[3] J. F. Moll, P. Akcora, A. Rungta, S. Gong, R. H. Colby, B. C. Benicewicz and S. K. Kumar, *Macromolecules*, 2011, **44**, 7473–7477.

[4] Z. Hao, A. Ghanekarade, N. Zhu, K. Randazzo, D. Kawaguchi, K. Tanaka, X. Wang, D. S. Simmons, R. D. Priestley and B. Zuo, *Nature*, 2021, **596**, 372–376.

[5] S. H. Chen, A. J. Souna, C. L. Soles, S. J. Stranick and E. P. Chan, *Soft Matter*, 2020, **16**, 3886–3890.

[6] J. Midya, M. Rubinstein, S. K. Kumar and A. Nikoubashman, *ACS Nano*, 2020, **14**, 15505–15516.

[7] E. P. Chan, W. Xie, S. V. Orski, J.-H. Lee and C. L. Soles, *ACS Macro Lett.*, 2019, **8**, 806–811.

[8] J. George, N. V. Sastry, S. R. Patel and M. K. Valand, *J. Chem. Eng. Data*, 2002, **47**, 262–269.

[9] R. P. Wool, *J. Polym. Sci. B Polym. Phys.*, 2005, **43**, 168–183.

[10] R. P. Wool, D. M. Bailey and A. D. Friend, *J. Adhes. Sci. Technol.*, 1996, **10**, 305–325.

[11] M. Rubinstein and R. H. Colby, *Polymer Physics*, Oxford University Press, USA, 1st edn, 2003.